Journal of Computational Physics **175,** 713–738 (2002)
doi:10.1006/jcph.2001.6964, available online at http://www.idealibrary.com on IDEAL®

Numerical Simulation of Isotropic Turbulence Using a Collocated Approach and a Nonorthogonal Grid System

A. Silva Lopes and J. M. L. M. Palma

Faculty of Engineering of University of Porto, Rua Dr. Roberto Frias, 4200-465 Porto, Portugal
E-mail: jpalma@fe.up.pt

Received July 12, 2000; revised October 22, 2001

We studied the effect of using a nonorthogonal grid coordinate system and a finite-volume approach in the simulation of decaying isotropic turbulence. Calculations were performed in distorted periodic cubic boxes and with a turbulent Reynolds number, based on the Taylor microscale and on a root mean square turbulent velocity, of approximately 40. A preliminary study showed that in the nonorthogonal grids some Fourier modes of the discretized derivatives can have greater amplitude or the phase inverted relatively to the modes of the exact derivative, contrary to what occurs with a Cartesian grid system. However, in the simulations, the statistical distributions of velocity, pressure, and longitudinal and lateral velocity derivatives were always identical, regardless of the grid distortion. The temporal evolution of the energy was also similar and the differences at the end of the simulations (after about two eddy turnover times) did not exceed 1%. Furthermore, the grid nonorthogonality affected neither the isotropy of the fields nor the correlation between the vorticity and the principal rates of strain. We concluded that the finite-volume approach in nonorthogonal grid systems may be used in the numerical simulation of complex turbulent flows with either the direct numerical simulation or large-eddy simulation methodologies.

Key Words: Isotropic turbulence; models; numerical methods.

1. INTRODUCTION

Direct numerical simulation (DNS) of turbulence is a major tool for fundamental studies and development or validation of turbulence closure theories [16, 20]. The work of Orszag and Patterson [18], on decaying isotropic turbulence, with turbulent Reynolds number based on the Taylor microscale (Re_λ) of approximately 40, is usually referred to as the first DNS study. Siggia [24] studies stationary forced turbulence ($Re_\lambda \approx 100$) with a subgrid like parametrization and reveals the existence of long and thin tubes of high vorticity. Kerr [11]

0021-9991/02 $35.00

studies high-order derivative correlations and the alignment between the principal rates of strain and the vorticity tubes. He concludes that the derivative correlations do not obey the scaling laws predicted by statistical models of intermittency and that the largest principal rate of strain is compressive and aligned perpendicularly to the vorticity tubes. Vincent and Meneguzzi [26] investigate the vorticity tubes and the statistics of velocity derivatives for $Re_\lambda \approx 150$, whereas the main interest of Métais and Lesieur [15] is on the decaying of stably stratified turbulence. Jiménez *et al.* [8] and Jiménez and Wray [7] study the dimensions and the velocity of the vorticity tubes, for $40 < Re_\lambda < 160$. All these studies use a uniform Cartesian mesh and pseudospectral methods, a combination usually considered to give the most accurate results for the computer resources available.

As computer performance increases and one realizes the limitations of closure theories based on Reynolds averaging Navier–Stokes (RaNS), the use of DNS and large-eddy simulations (LES) in real engineering applications has become more appealing (see, for instance, Ref. [1]). However, real engineering applications require coordinate systems with high geometric flexibility, which precludes the utilization of either uniform Cartesian meshes or pseudospectral methods, and requires techniques which are still relatively uncommon to the DNS/LES community (finite differences, finite element, etc.). Because in terms of numerical accuracy DNS and LES are more demanding than RaNS-based codes, a consistent analysis of numerical errors introduced by the utilization of different techniques is needed.

A simple choice, which some works have pursued, is to test the techniques of the engineering applications in basic turbulent flows. Rai and Moin [19], for instance, suggest the utilization of a fourth-order-accurate method to obtain results with the same accuracy as a pseudospectral method in the DNS of a channel flow. Ghosal [5] presents results of isotropic turbulence and analyzes the relative magnitude of the subgrid stresses and truncation and aliasing errors. Kravchenko and Moin [13] consider the flow inside a channel; they find that the errors can be of the same order as the subgrid stresses, that truncation errors are more important for low-order methods, and that aliasing errors are more important for high-order or spectral methods. Kaltenbach [10] studies the influence in the anisotropy of the resolved and subgrid stresses of an anisotropic filter, a consequence of the utilization of a grid with different spaces in each direction. He concludes that the effect depends on parameters like the grid anisotropy, the resolved scales, and the energy spectra shape near the small resolved scales.

The major goal of our work was to study the suitability of a nonorthogonal mesh in terms of both spatial and temporal accuracy. This was a first step in the development of computer codes based on either the DNS or LES methodologies for flow simulation in complex geometries [9]. As a test case for our study we selected the decay of three-dimensional isotropic turbulence. We considered the same case as did Orszag and Patterson [18], but in a distorted domain. Despite being almost 30 years old, this study's simplicity made it the most appealing in the context of our work, since we were interested only in the major parameters of isotropic turbulence. The decaying (nonstationary) isotropic turbulence was preferred to stationary turbulence because the forcing mechanism could be avoided.

The following text is divided into three sections. In Section 2 we present the mathematical model, the numerical techniques, and the procedure that we followed to generate the initial fields. An analysis of the errors of the discretized derivatives, the results of the simulations, and the corresponding discussion are presented in Section 3. Section 4 concludes the article and summarizes our main conclusions.

2. MODEL

2.1. Mathematical Model

The continuity equation,

$$\frac{\partial \rho u_i}{\partial x_i} = 0, \tag{1}$$

and the Navier–Stokes equation,

$$\frac{\partial \rho u_i}{\partial t} + \frac{\partial (\rho u_j u_i)}{\partial x_j} = \frac{\partial \tau_{ij}}{\partial x_j} - \frac{\partial p}{\partial x_i}, \tag{2}$$

were discretized using the finite-volume approach in a nonorthogonal and nonstaggered grid, second-order central differences for spatial discretization, and a third-order Runge–Kutta scheme for time discretization. In Eqs. (1) and (2) u_i are the velocity components along the coordinates x_i, p is the pressure, ρ is the fluid density, t is the time, and τ_{ij} are the stress tensor components.

The continuity equation (1) integrated over the control volume Ω,

$$\int_{\Omega} \frac{\partial \rho u_i}{\partial x_i} \, \mathrm{d}\Omega = 0, \tag{3}$$

according to Gauss' divergence theorem yields

$$\int_S \rho \boldsymbol{v} \cdot \boldsymbol{n} \, \mathrm{d}S = \sum_l \int_{S_l} \rho \boldsymbol{v} \cdot \boldsymbol{n} \, \mathrm{d}S = \sum_i \dot{m}_l, \quad l = \mathrm{e},\ \mathrm{w},\ \mathrm{n},\ \mathrm{s}, \ldots. \tag{4}$$

In our nomenclature (cf. Ref. [4]), $\boldsymbol{v}$ is the velocity vector, $\boldsymbol{n}$ is the unit vector normal to surface S, the subscript l stands for each of the six faces of the control volume (identified as east, west, north, south, top, and bottom), and $\dot{m}_l$ is the mass flux across each face.

The Navier–Stokes equation (2) in finite-volume formulation is

$$\frac{\partial}{\partial t} \int_{\Omega} \rho u_i \, \mathrm{d}\Omega + \int_S \rho u_i \boldsymbol{v} \cdot \boldsymbol{n} \, \mathrm{d}S = \int_S \tau_{ij} \boldsymbol{i_j} \cdot \boldsymbol{n} \, \mathrm{d}S - \int_S p \boldsymbol{i_i} \cdot \boldsymbol{n} \, \mathrm{d}S, \tag{5}$$

where $\boldsymbol{i_j}$ is the coordinate vector along direction x_j. The discretization of the convective term is

$$\int_S \rho u_i \boldsymbol{v} \cdot \boldsymbol{n} \, \mathrm{d}S = \sum_l \int_{S_l} \rho u_i \boldsymbol{v} \cdot \boldsymbol{n} \, \mathrm{d}S = \sum_l F^{\mathrm{a}}_{i,l}, \quad l = \mathrm{e}, \mathrm{w}, \mathrm{n}, \mathrm{s}, \ldots. \tag{6}$$

The convective flux across the east surface, for instance, is given by

$$F^{\mathrm{a}}_{i,\mathrm{e}} = \int_{S_\mathrm{e}} \rho u_i \boldsymbol{v} \cdot \boldsymbol{n} \, \mathrm{d}S \approx \dot{m}_\mathrm{e} u_{i,\mathrm{e}},$$

where the velocity at the face of the control volume ($u_{i,\mathrm{e}}$) is obtained by linear interpolation.

The discretization of the diffusive term is

$$\int_S \tau_{ij}\boldsymbol{i_j}\cdot\boldsymbol{n}\,\mathrm{d}S = \sum_l \int_{S_l} \tau_{ij}\boldsymbol{i_j}\cdot\boldsymbol{n}\,\mathrm{d}S = \sum_l F^{\mathrm{d}}_{i,l}, \quad l = \mathrm{e, w, n, s, \ldots}. \tag{7}$$

The diffusive flux across the east face, $F^{d}_{i,\mathrm{e}}$, is defined by

$$F^{\mathrm{d}}_{i,\mathrm{e}} = \int_{S_\mathrm{e}} \tau_{ij}\boldsymbol{i_j}\cdot\boldsymbol{n}\,\mathrm{d}S \approx (\tau_{ij})_\mathrm{e} S^j_\mathrm{e}.$$

To calculate the stresses we used a local coordinate transformation, defined by $x_i = x_i(\xi_j)$, $j = 1, 2, 3$ and characterized by the Jacobian J:

$$J = \det\left(\frac{\partial x_i}{\partial \xi_j}\right) = \begin{vmatrix} \dfrac{\partial x}{\partial \xi} & \dfrac{\partial x}{\partial \eta} & \dfrac{\partial x}{\partial \zeta} \\ \dfrac{\partial y}{\partial \xi} & \dfrac{\partial y}{\partial \eta} & \dfrac{\partial y}{\partial \zeta} \\ \dfrac{\partial z}{\partial \xi} & \dfrac{\partial z}{\partial \eta} & \dfrac{\partial z}{\partial \zeta} \end{vmatrix}. \tag{8}$$

Using this transformation, the derivatives of any variable ϕ with respect to the Cartesian directions were calculated using

$$\frac{\partial \phi}{\partial x_i} = \frac{\partial \phi}{\partial \xi_j}\frac{\partial \xi_j}{\partial x_i} = \frac{\partial \phi}{\partial \xi_j}\frac{\beta^{ij}}{J}, \tag{9}$$

where β^{ij} is the cofactor of $\partial x_i/\partial \xi_j$ in the Jacobian J. $\boldsymbol{S}$, the surface vector of the control volume, is defined at the east face by

$$\boldsymbol{S}_\mathrm{e} = S_\mathrm{e}\boldsymbol{n} = S^x_\mathrm{e}\boldsymbol{i} + S^y_\mathrm{e}\boldsymbol{j} + S^z_\mathrm{e}\boldsymbol{k},$$

where each component can be written as a function of the cofactors β^{ij}:

$$S^x_\mathrm{e} = \beta^{11}_\mathrm{e}\Delta\eta\Delta\zeta, \quad S^y_\mathrm{e} = \beta^{21}_\mathrm{e}\Delta\xi\Delta\zeta, \quad \text{and} \quad S^z_\mathrm{e} = \beta^{31}_\mathrm{e}\Delta\xi\Delta\eta.$$

Under these conditions and for a Newtonian fluid, the stress tensor components at the east face and for the u velocity, for instance, are the

$$(\tau_{xx})_\mathrm{e} \approx 2\frac{\mu}{J_\mathrm{e}}\left[\frac{u_\mathrm{E}-u_\mathrm{P}}{\Delta\xi}\beta^{11}_\mathrm{e} + \left(\frac{\delta u}{\delta\eta}\beta^{12}\right)_\mathrm{e} + \left(\frac{\delta u}{\delta\zeta}\beta^{13}\right)_\mathrm{e}\right],$$

$$(\tau_{xy})_\mathrm{e} \approx \frac{\mu}{J_\mathrm{e}}\left[\frac{v_\mathrm{E}-v_\mathrm{P}}{\Delta\xi}\beta^{11}_\mathrm{e} + \left(\frac{\delta v}{\delta\eta}\beta^{12}\right)_\mathrm{e} + \left(\frac{\delta v}{\delta\zeta}\beta^{13}\right)_\mathrm{e} + \frac{u_\mathrm{E}-u_\mathrm{P}}{\Delta\xi}\beta^{21}_\mathrm{e} + \left(\frac{\delta u}{\delta\eta}\beta^{22}\right)_\mathrm{e} + \left(\frac{\delta u}{\delta\zeta}\beta^{23}\right)_\mathrm{e}\right],$$

$$(\tau_{xz})_\mathrm{e} \approx \frac{\mu}{J_\mathrm{e}}\left[\frac{w_\mathrm{E}-w_\mathrm{P}}{\Delta\xi}\beta^{11}_\mathrm{e} + \left(\frac{\delta w}{\delta\eta}\beta^{12}\right)_\mathrm{e} + \left(\frac{\delta w}{\delta\zeta}\beta^{13}\right)_\mathrm{e} + \frac{u_\mathrm{E}-u_\mathrm{P}}{\Delta\xi}\beta^{31}_\mathrm{e} + \left(\frac{\delta u}{\delta\eta}\beta^{32}\right)_\mathrm{e} + \left(\frac{\delta u}{\delta\zeta}\beta^{33}\right)_\mathrm{e}\right],$$

where the derivatives at the face of the control volume ($\delta\phi/\delta\eta$ and $\delta\phi/\delta\zeta$) are obtained by linear interpolation of the derivatives at the center.

Finally, the discretization of the pressure gradient term yields

$$Q_i^p = -\int_S p\boldsymbol{i}_i \cdot \boldsymbol{n}\,\mathrm{d}S \approx -\sum_l p_l S_l^i, \quad l = \mathrm{e, w, n, s, \ldots}, \tag{10}$$

where the pressure at the faces of the control volume is obtained also by linear interpolation.

The set of equations above describes the fluid flow equations (1) and (2) as implemented in our computer code. Because no explicit subgrid model was used, our calculations are classified as DNS.

2.2. Numerical Techniques

To solve Eqs. (1) and (2) we used a semi-implicit algorithm based on the fractional step method of Kim and Moin [12], which comprised the time integration of the momentum equation (step 1) and the implicit solution of a Poisson equation for the pressure, to guarantee a divergence-free velocity field (step 2).

After spatial discretization, followed by time discretization, Eq. (2) reads

$$(\rho u_i)^{*n+1} - (\rho u_i)^n = \int_{t_n}^{t_{n+1}} \left[-\frac{\delta(\rho u_j u_i)}{\delta x_j} + \frac{\delta \tau_{ij}}{\delta x_j} \right]_i \mathrm{d}t. \tag{11}$$

The integral was solved by the Runge-Kutta (4,3) scheme (see Appendix or Ref. [3] for further details). Our choice of the Runge-Kutta (4,3) scheme for temporal discretization was based on the results of a preliminary study [25], using five different alternative schemes for temporal discretization. Again, using the east face as an example, the mass flow rate after step 1 was found using

$$\dot{m}_\mathrm{e}^{*n+1} = \rho_\mathrm{e} \sum_i \overline{\left(u_i^{*n+1}\right)}_\mathrm{e} S_\mathrm{e}^i,$$

where the overscore indicates an interpolation over nodes P and E and the asterisk refers to a velocity field that may violate mass conservation.

The objective of step 2 of the algorithm is to correct the velocity field u_i^{*n+1} in such a way that mass conservation is satisfied at each control volume. This is achieved via a pressure field obtained by solution of the Poisson equation

$$\sum_l \rho_l \Delta t S_l^i \frac{\delta p^{n+1}}{\delta x_i} = \sum_l \dot{m}_l^{*n+1}, \quad l = \mathrm{e,\ w,\ n,\ s, \ldots}, \tag{12}$$

which was solved using a mixed spectral/Gaussian elimination solver.

After, the velocities are corrected using

$$(\rho u_i)^{n+1} = (\rho u_i^*)^{n+1} - \Delta t \frac{\delta p^{n+1}}{\delta x_i}$$

and the mass flux at the east face, for instance, is corrected using

$$\dot{m}_\mathrm{e}^{n+1} = \dot{m}_\mathrm{e}^{*n+1} - \rho_\mathrm{e} \Delta t \sum_i S_\mathrm{e}^i \left(\frac{\delta p^{n+1}}{\delta x_i} \right)_\mathrm{e}. \tag{13}$$

This procedure of calculating the mass flux was originally proposed by Rhie and Chow [21] for orthogonal collocated grids. Though avoiding the occurrence of oscillations in the pressure, it yields a loss of conservation of kinetic energy proportional to the cell surface area and of order $\Delta t \cdot \Delta$ (Δ is the mesh spacing). (For a more detailed analysis on this aspect, see, for instance, Refs. [4, 17]). This disadvantage of collocated grids compared with staggered grids is not enough to preclude their use. Because they enable a simpler treatment, collocated grids are usually preferred in the case of nonorthogonal coordinate systems and complex geometries, even for large-eddy simulations (e.g., Refs. [2, 27]).

3. RESULTS AND DISCUSSION

This section, which presents and discusses the results, is divided into five subsections. The section begins with a description of the test conditions (Section 3.1). The effects of the grid nonorthogonality on the discretized derivative with respect to the Cartesian direction z, using a second- or a fourth-order centered finite-difference scheme are analyzed in Section 3.2. Because the effect of the nonorthogonal terms could influence different aspects of the flow, the results were analyzed at the beginning and at the end of the simulations (Sections 3.3 and 3.5). Section 3.4 focuses on the temporal evolution of the statistical parameters during two eddy turnover times.

3.1. Test Conditions

The physical domain of the reference case (orthogonal) was a periodic cubic box of side length $\ell = \pi$ cm, which was discretized by meshes with 64^3 and 128^3 grid points. It is generally accepted (e.g., Refs. [6, 18]) that the accuracy of finite-difference calculations is comparable to spectral calculation with half the number of nodes along each direction. The time step (Δt) of the temporal discretization was 0.004 and 0.002 s, for 64^3 and 128^3 grids, respectively. The kinematic viscosity was $\nu = 0.01189$ cm^2/s, as in Orszag and Patterson [18], leading to a Reynolds number based on the Taylor microscale ($Re_\lambda = v_{\text{rms}}\lambda/\nu$) of approximately 40.

To study nonorthogonality effects, calculations were also performed in distorted cubic boxes, where the computational directions ξ and η were coincident with the physical directions x and y. The angle α, between the physical direction z and the computational direction ζ, was varied between 0 and 45°, in steps of 15°, in the xz Cartesian plane (Fig. 1). In this case, the tensor β/J was

$$\frac{\beta}{J} = \frac{1}{\Delta}\begin{bmatrix} 1 & 0 & 0 \\ 0 & 1 & 0 \\ -\tan\alpha & 0 & 1 \end{bmatrix}, \tag{14}$$

where $\Delta = \ell/N$ is the mesh space in the orthogonal domain, with N being the number of nodes in each direction. The volume of the domains with inclined boundaries was the same as the original because no other distortion was applied. Periodic boundary conditions are still applied in the Cartesian directions. The orthogonal domain and the domain with a 30° angle between z and ζ are shown in Fig. 2. Note that although in mathematical terms only one direction was affected, during the course of the calculations other directions could also be affected. The direction of our choice was irrelevant given the turbulence isotropy and the lack of mean shear.

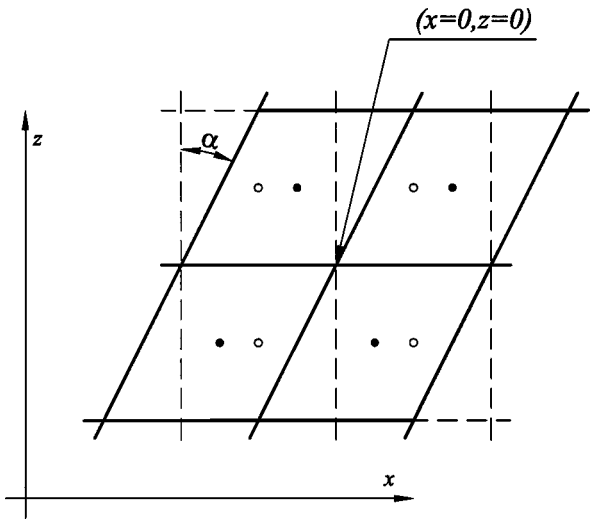

FIG. 1. Control volume in grids with angles of 0° and α between z and ζ.

The initial flow field was an isotropic Gaussian centered (zero mean) random ensemble with the energy spectrum

$$E(k) = Ak^4 \exp(-Bk^2), \tag{15}$$

where k is the wave number. A and B were chosen so that $\int E(k)\,\mathrm{d}k = 3/2\ (\mathrm{cm/s})^2$ and the maximum of $E(k)$ occurred at $k_\mathrm{p} = 2^{9/4}\ \mathrm{cm}^{-1}$.

In the orthogonal grid, the initial fields were generated using the methodology described in Ref. [22]. The same methodology was also used for the nonorthogonal grids, but without enforcing continuity during the construction in the wave number space. For each wave

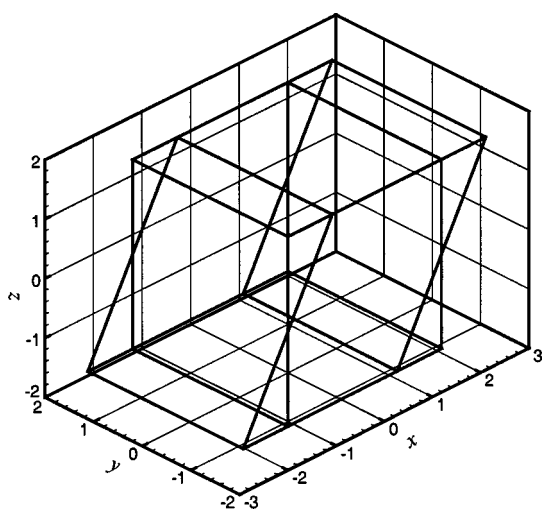

FIG. 2. Physical domains with 0 and 30° angles between z and ζ.

number vector

$$k_{l,m,n} = \frac{2\pi}{l}(l, m, n), \quad l, m, n = -N/2, \ldots, 0, \ldots, N/2 - 1,$$

there is a Fourier mode $\hat{\boldsymbol{u}}^*_{i,m,n} = \hat{\boldsymbol{u}}^*(\boldsymbol{k}_{l,m,n})$. The velocity field in the Cartesian space $\boldsymbol{u}^*_{i,j,k} = \boldsymbol{u}^*(\boldsymbol{x}_{i,j,k})$ is obtained by the inverse transform

$$\boldsymbol{u}^*_{i,j,k} = \sum_{l,m,n} \hat{\boldsymbol{u}}^*_{l,m,n} \exp(i\boldsymbol{k}_{l,m,n} \cdot \boldsymbol{x}_{i,j,k}). \tag{16}$$

The grid node locations are given by

$$\boldsymbol{x}_{i,j,k} = \frac{\ell}{N}\left(i - \frac{N+1}{2} + \left(k - \frac{N+1}{2}\right)\tan\alpha,\ j - \frac{N+1}{2},\ k - \frac{N+1}{2}\right), \quad i, j, k, = 1, \ldots, N. \tag{17}$$

The continuity was enforced only after the transformation to the physical space (i.e. $\boldsymbol{u}^*$ is the velocity field immediately after the transformation, which only satisfies continuity after the correction $\boldsymbol{u} = \boldsymbol{u}^* - \boldsymbol{\nabla}\phi$, where ϕ is the solution of the Poisson equation $\nabla^2\phi = \boldsymbol{\nabla} \cdot \boldsymbol{u}^*$).

For every domain (or distortion) three computer simulations were performed with the 64^3 grid and one run with the 128^3 grid. The three computer simulations differed only by the seed of the random-number generator and the same seeds were used in all domains, in order to obtain identical initial fields. All calculations were done on single precision (four-byte length for a real), because tests done on double precision (eight-byte length for a real) did not show any significant difference.

3.2. Influence of the Grid Nonorthogonality on the Discretized Derivatives

Consider the Fourier series of a generic variable ϕ,

$$\phi_{i,j,k} = \sum_{l,m,n} \hat{\phi}_{l,m,n} \exp(i\boldsymbol{k}_{l,m,n} \cdot \boldsymbol{x}_{i,j,k}),$$

where $\boldsymbol{x}_{i,j,k}$ are the grid points.

The Fourier series for the derivative $\partial\phi/\partial z$ is given by

$$\left(\frac{\partial\phi}{\partial z}\right)_{i,j,k} = \sum_{l,m,n} ik_z\hat{\phi}_{l,m,n} \exp(i\boldsymbol{k}_{l,m,n} \cdot \boldsymbol{x}_{i,j,k}).$$

However, when the derivatives are discretized, this expansion is obtained only if a spectral method is used. To study the effect of the discretization by finite differences in a nonorthogonal mesh, we defined

$$Q = \frac{(\widehat{\delta\phi/\delta z})_{l,m,n}}{(\widehat{\partial\phi/\partial z})_{l,m,n}},$$

the ratio between the Fourier modes of the derivative discretized by finite differences $(\widehat{\delta\phi/\delta z})$ and the modes of the exact derivative $(\widehat{\partial\phi/\partial z})$. If $Q < 0$, the Fourier modes of the discretized

derivative are in opposite phase to the Fourier modes of the exact derivative. Depending on whether $|Q| < 1$ or $|Q| > 1$, the amplitude of the Fourier modes of the exact derivative is reduced or increased by the finite-difference discretization. For higher accuracy of the finite-difference discretization, Q should be close to 1.

The dependency of Q on the wave number was studied for grid distortions of 0 (orthogonal), 15, 30, and 45°, for either second- or fourth-order-accurate central difference schemes. However, the actual calculations were all done with a second-order-accurate scheme.

3.2.1. *Second-Order-Accurate Finite Central Differences*

It follows from the mathematical model presented in Section 2 that the discretization of $\partial\phi/\partial z$ involves the discretization of $\partial\phi/\partial\xi$ and $\partial\phi/\partial\zeta$:

$$\left(\frac{\delta\phi}{\delta\xi}\right)_{i,j,k} = \frac{\phi_{i+1,j,k} - \phi_{i-1,j,k}}{2}, \tag{18}$$

$$\left(\frac{\delta\phi}{\delta\zeta}\right)_{i,j,k} = \frac{\phi_{i,j,k+1} - \phi_{i,j,k-1}}{2}. \tag{19}$$

Equations (18) and (19) are second-order approximations and we considered $\Delta\xi = \Delta\zeta = 1$. Using the translation property of the Fourier series and because $\exp(i\theta) - \exp(-i\theta) = 2i\sin\theta$, the Fourier series for these derivatives are

$$\left(\frac{\delta\phi}{\delta\xi}\right)_{i,j,k} = \sum_{l,m,n} i\sin(k_x\Delta)\hat{\phi}_{l,m,n}\exp(i\boldsymbol{k}_{l,m,n}\cdot\boldsymbol{x}_{i,j,k}),$$

$$\left(\frac{\delta\phi}{\delta\zeta}\right)_{i,j,k} = \sum_{l,m,n} i\sin(k'_z\Delta)\hat{\phi}_{l,m,n}\exp(i\boldsymbol{k}_{l,m,n}\cdot\boldsymbol{x}_{i,j,k}),$$

where

$$k'_z = k_x\tan\alpha + k_z.$$

After the coordinate transformation (9), the series for the discretized derivative with respect to the Cartesian direction z is obtained:

$$\left(\frac{\delta\phi}{\delta z}\right)_{i,j,k} = \sum_{l,m,n} i\frac{\sin(k'_z\Delta) - \sin(k_x\Delta)\tan\alpha}{\Delta}\hat{\phi}_{l,m,n}\exp(i\boldsymbol{k}_{l,m,n}\cdot\boldsymbol{x}_{i,j,k}). \tag{20}$$

When $\alpha \neq 0$, apart from k_z, (20) depends also on k_x and $\tan\alpha$. Note that in a more general case every derivative would depend on all wave numbers and angles between the Cartesian (x, y, and z) and the computational directions (ξ, η, and ζ).

Defining the maximum wave number on a grid with mesh spacing $\Delta(k_{\max} = \pi/\Delta)$ and normalizing the wave numbers

$$k_x^* = \frac{k_x}{k_{\max}}, \tag{21}$$

$$k_z^* = \frac{k_z}{k_{\max}}, \tag{22}$$

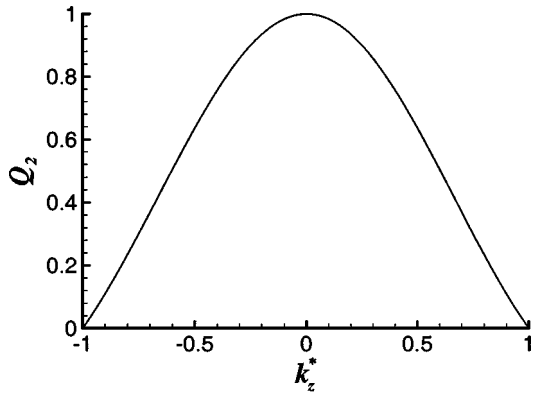

FIG. 3. Ratio (Q_2) between the amplitudes of the Fourier modes of the discretized derivative (using second-order central differences) and the amplitudes of the Fourier modes of the exact derivative on the orthogonal mesh ($\alpha = 0^\circ$), as a function of the normalized wave number.

Q_2, the ratio between the Fourier modes of the discretized and the Fourier modes of the exact derivative for a second-order-accuracy finite-difference scheme, is given by

$$Q_2 = \frac{\sin(k_z^{*\prime}\pi) - \sin(k_x^*\pi)\tan\alpha}{k_z^*\pi}, \tag{23}$$

where $k_z^{*\prime} = k_x^* \tan\alpha + k_z^*$ and $k_x^*, k_z^* \in [-1, 1[$.

In case of an orthogonal grid ($\alpha = 0^\circ$), Q_2 is a function of k_z^* only and varies as illustrated in Fig. 3. The result is by no means surprising, though in a graphical representation different from that used by, for instance, Refs. [13, 14]. Figure 3 shows the difficulty of the finite-difference scheme in resolving the higher wave numbers and the improved accuracy as the wave number approaches zero (i.e. Q_2 approaches 1).

For a nonorthogonal mesh ($\alpha \neq 0$), because Q_2 is a function of both k_z^* and k_x^*, we decided to display this two-variable function as a contour map (Fig. 4). Contrary to the orthogonal case, Q_2 could be negative on any of the nonorthogonal grids. For $\alpha = 15$ and 30°, Q_2 was not limited and continuous when $k_x^* \neq 0$ and $k_z^* = 0$ (Figs. 4a and 4b). Under these conditions, Q_2 tends to positive or negative infinite values, depending on the algebraic sign of k_x^* and on whether $k_z^* \to 0^+$ or $k_z^* \to 0^-$. When $\alpha = 45^\circ$, because $\tan\alpha = 1$, Q_2 was continuous and limited (Fig. 4c).

Figures 3 and 4 show Q_2 as a continuous function of one or two of the components of the wave number vector. It is also important to know how the discrete set of simulated modes in a given grid are affected. Figures 5 and 6 show the minimum, average, and maximum values of Q_2 in the two grids used in the simulations (with 64^3 and with 128^3 grid nodes), functions of the wave number vector length. The gain of accuracy obtained by doubling the number of grid nodes in each direction is visible by comparing the minimum, average, and maximum values of Q_2 for $k < 64$ in the two grids. Due to the discontinuity in Q_2 when $k_x^* \neq 0, k_z^* = 0$, and $\alpha = 15$ or 30°, the minimum and maximum values for $\alpha = 15$ and 30° were much greater than for $\alpha = 0$ or 45° and they could be greater in the grid with 128^3 nodes than in the grid with 64^3 nodes. The average value, however, was less affected by the grid distortion: it was about 0.6 for the highest wave numbers in

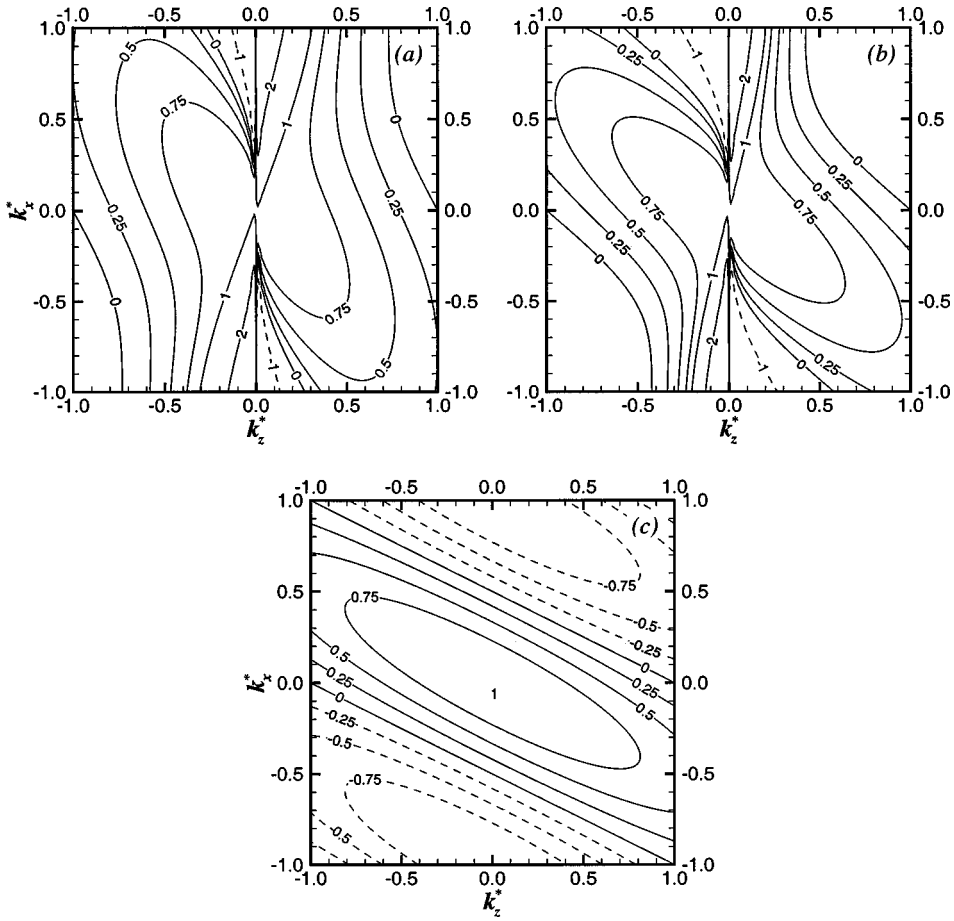

FIG. 4. Ratio (Q_2) between the amplitudes of the Fourier modes of the discretized derivative (using second-order central differences) and the amplitudes of the Fourier modes of the exact derivative, as a function of the normalized wave number. (a) $\alpha = 15^\circ$; (b) $\alpha = 30^\circ$; (c) $\alpha = 45^\circ$.

the Cartesian grid and decreased with increasing grid distortion, until it reached -0.1 for $\alpha = 45^\circ$.

3.2.2. *Fourth-Order-Accurate Finite Central Differences*

In the case of fourth-order-accurate scheme finite central differences, the derivatives $\partial\phi/\partial\xi$ and $\partial\phi/\partial\zeta$ are given by

$$\left(\frac{\delta\phi}{\delta\xi}\right)_{i,j,k} = \frac{-\phi_{i+2,j,k} + 8\phi_{i+1,j,k} - 8\phi_{i-1,j,k} + \phi_{i-2,j,k}}{12}, \tag{24}$$

$$\left(\frac{\delta\phi}{\delta\zeta}\right)_{i,j,k} = \frac{-\phi_{i,j,k+2} + 8\phi_{i,j,k+1} - 8\phi_{i,j,k-1} + \phi_{i,j,k-2}}{12}. \tag{25}$$

Using the translation property of the Fourier series, and because $\exp(i\theta) - \exp(-i\theta) = 2i\sin\theta$ and $\exp(i\theta) + \exp(-i\theta) = 2\cos\theta$, the Fourier series for derivatives (24) and (25)

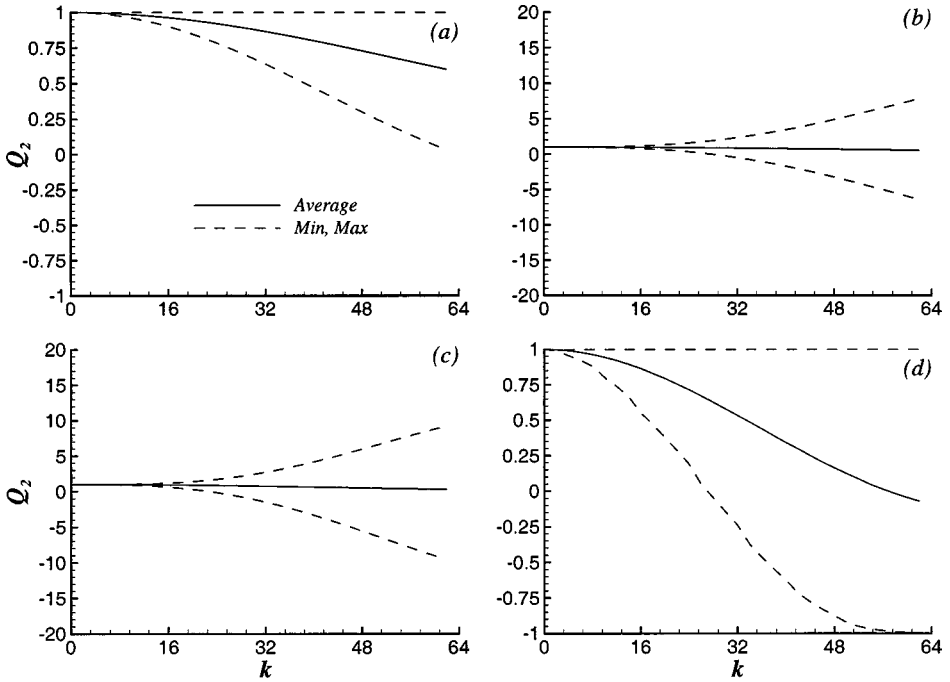

FIG. 5. Minimum, average, and maximum ratio (Q_2) between the amplitudes of the Fourier modes of the discretized derivative in the grid with 64^3 grid nodes (using second-order central differences) and the amplitudes of the Fourier modes of the exact derivative, as a function of the wave number vector length. (a) $\alpha = 0^\circ$; (b) $\alpha = 15^\circ$; (c) $\alpha = 30^\circ$; (d) $\alpha = 45^\circ$. Note that the vertical scales in (a) and (d) are different from those in (b) and (c).

are

$$\left(\frac{\delta\phi}{\delta\xi}\right)_{i,j,k} = \sum_{l,m,n} i\frac{\sin(k_x\Delta)}{3}[4-\cos(k_x\Delta)]\hat{\phi}_{l,m,n}\exp(i\boldsymbol{k}_{l,m,n}\cdot\boldsymbol{x}_{i,j,k}),$$

$$\left(\frac{\delta\phi}{\delta\zeta}\right)_{i,j,k} = \sum_{l,m,n} i\frac{\sin(k'_x\Delta)}{3}[4-\cos(k'_x\Delta)]\hat{\phi}_{l,m,n}\exp(i\boldsymbol{k}_{l,m,n}\cdot\boldsymbol{x}_{i,j,k}).$$

The Fourier series for the derivative with respect to the Cartesian direction z is given by

$$\left(\frac{\delta\phi}{\delta z}\right)_{i,j,k} = \sum_{l,m,n} i\left\{\frac{\sin(k'_z\Delta)}{3\Delta}[4-\cos(k'_z\Delta)] - \frac{\sin(k_x\Delta)}{3\Delta}[4-\cos(k_x\Delta)]\tan\alpha\right\}\hat{\phi}_{l,m,n}\exp(i\boldsymbol{k}_{l,m,n}\cdot\boldsymbol{x}_{i,j,k}).$$

Using the wave number normalization (21) and (22), the ratio Q_4 between the Fourier modes of the discretized and the exact derivative is

$$Q_4 = \frac{\sin(k_z^{*\prime}\pi)[4-\cos(k_z^{*\prime}\pi)] - \sin(k_x^*\pi)[4-\cos(k_x^*\pi)]\tan\alpha}{3k_z^*\pi}. \tag{26}$$

Figure 7 shows this relation for an orthogonal mesh which, when compared with Fig. 3,

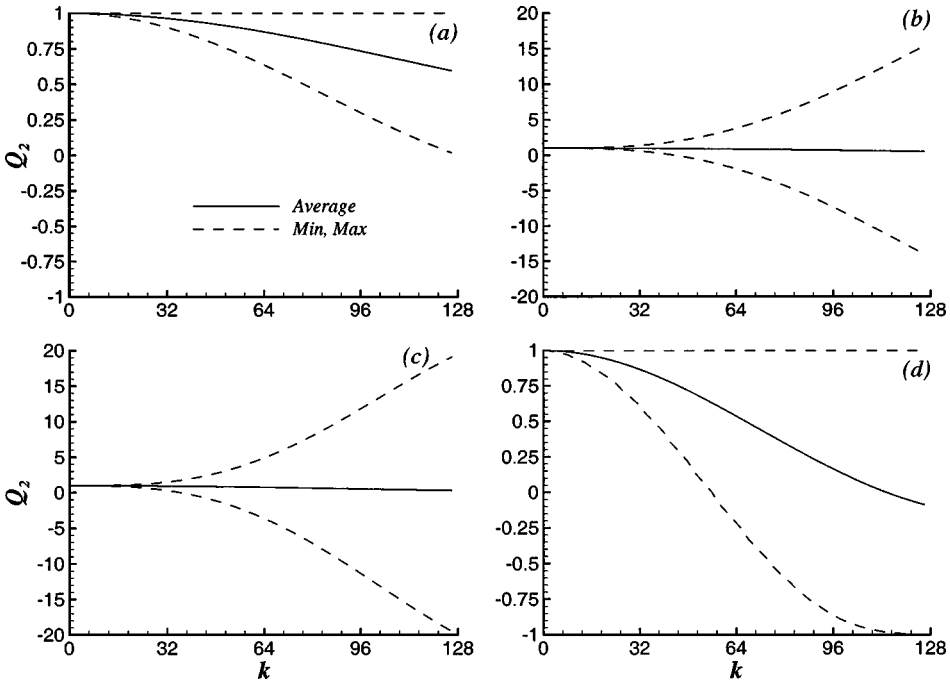

FIG. 6. Minimum, average, and maximum ratio (Q_2) between the amplitudes of the Fourier modes of the discretized derivative in the grid with 128^3 grid nodes (using second-order central differences) and the amplitudes of the Fourier modes of the exact derivative, as a function of the wave number vector length. (a) $\alpha = 0°$; (b) $\alpha = 15°$; (c) $\alpha = 30°$; (d) $\alpha = 45°$. Note that the vertical scales in (a) and (d) are different from those in (b) and (c).

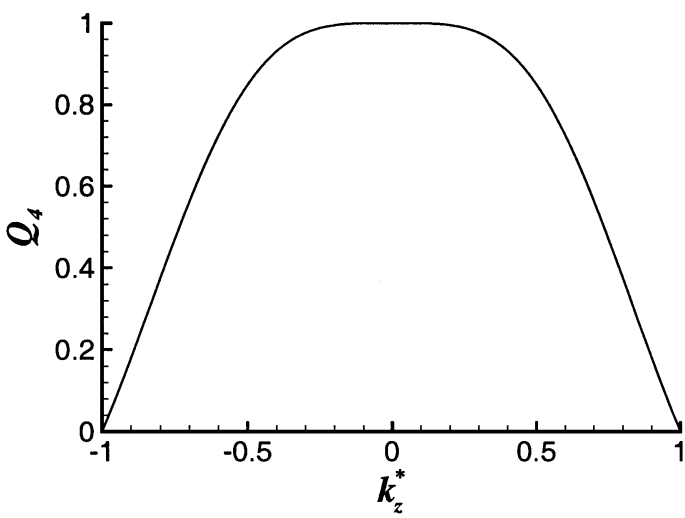

FIG. 7. Ratio (Q_4) between the amplitudes of the Fourier modes of the discretized derivative (using fourth-order central differences) and the amplitudes of the Fourier modes of the exact derivative on the orthogonal mesh ($\alpha = 0°$), as a function of the normalized wave number.

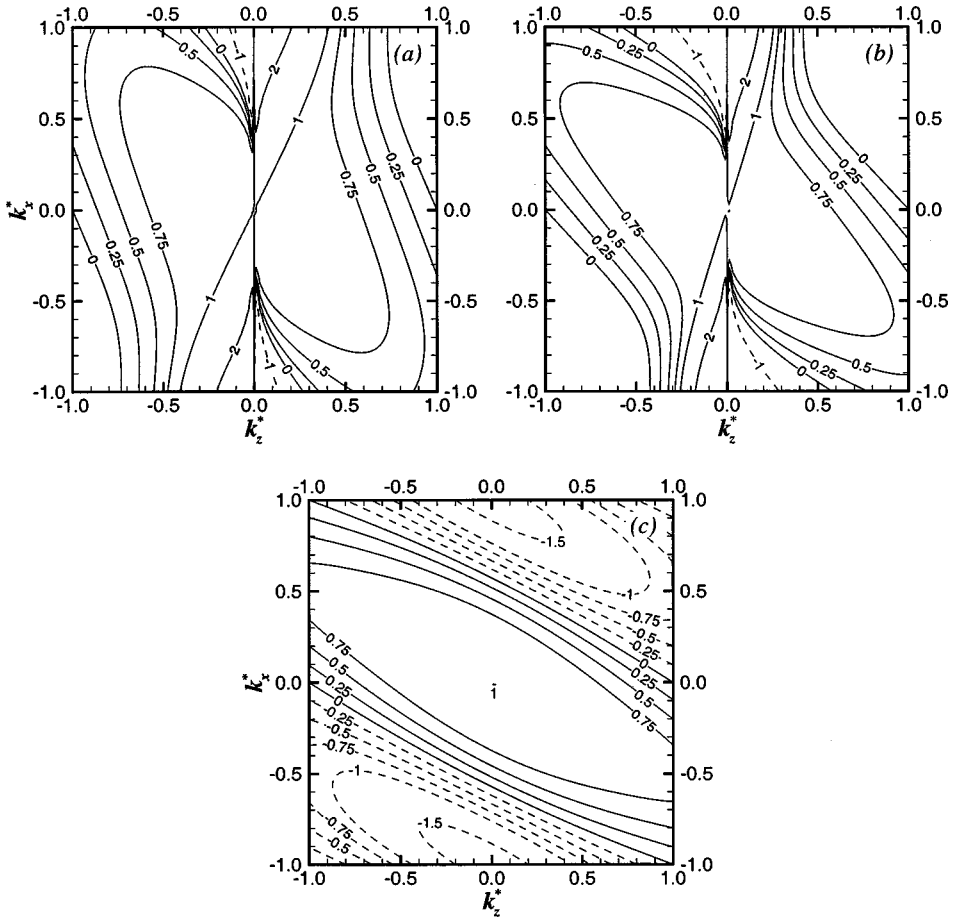

FIG. 8. Ratio (Q_4) between the amplitudes of the Fourier modes of the discretized derivative (using fourth-order central differences) and the amplitudes of the Fourier modes of the exact derivative, as a function of the normalized wave number. (a) $\alpha = 15^\circ$; (b) $\alpha = 30^\circ$; (c) $\alpha = 45^\circ$.

shows a wider range of k_z^*, for which Q_4 stays close to 1. Lele [14] quantifies the resolution characteristics of various finite-difference schemes and shows that for $Q > 0.9, 25$ or 44% of the wave number range is well resolved for a second- or a fourth-order scheme.

On the nonorthogonal meshes, the contour shapes of Q_4 (Fig. 8) were similar to Q_2 (Fig. 4); however, the area covered by the conditions $0.75 < Q_4 < 1$ and $|Q_4| > 1$ was larger compared with the second-order scheme. If the enlargement of $0.75 < Q < 1$ improves the accuracy, the enlargement of $|Q| > 1$ degrades it. However, because no simulations were made using the fourth-order scheme, we could not say which one was the prevailing effect. As in case of Q_2, for $\alpha = 15$ or 30°, Q_4 was not limited and was discontinuous when $k_x^* \neq 0$ and $k_z^* = 0$.

It is expected that, with a fourth-order scheme, the grid refinement also improves the accuracy of the results. However, that is not certain in the case of $\alpha = 45^\circ$ (Fig. 8). For instance, a mode with $k_x^* = k_z^* = 0.9$ where $Q_4 = -0.4$ after grid refinement such that $k_x^* = k_z^* = 0.6$ has $Q_4 = -1.2$ and the global accuracy may or may not improve.

3.3. Initial Fields

Because the procedure that we used to generate the initial fields (see Section 3.1) had never been applied to nonorthogonal grids, we first investigated whether the initial fields were identical and had the intended characteristics of isotropy and Gaussian distribution, regardless of the grid distortion. For isotropy indicators, we used the distribution of fluctuations of velocity and vorticity between the three Cartesian components (related to the isotropy of the large and small scales, respectively) and the isotropic relation

$$\frac{\langle \omega^2 \rangle}{\langle \mathrm{tr}(s^2) \rangle} = 2, \tag{27}$$

where the operator $\langle \cdots \rangle$ denotes an ensemble average, ω is the vorticity, $s_{ij} = 1/2(\partial u_j/\partial x_i + \partial u_i/\partial x_j)$ is the rate of strain tensor, and $\mathrm{tr}(s^2) = \sum s_{ij} s_{ji}$. These parameters are displayed in Table I: three simulations with the 64^3 grid for each domain distortion and one with the 128^3 grid (see Section 3.1).

The distribution of the velocity or vorticity fluctuations between the three Cartesian components was not affected by the grid distortion (Table I). The small variations between identical runs in domains with different distortion were not significant and were attributed to numerical discretization.

In the orthogonal and in the 15° domains, the isotropic relation (27) was satisfied up to the third decimal figure (i.e. within less than 0.05%). There was a tendency to lose isotropy with greater distortions, due to the correction to satisfy continuity, but the maximum error was only 0.15%. Note that this tendency did not exist with the finer grid.

The statistical distributions of the velocity and its longitudinal and lateral derivatives ($\partial u/\partial x$ and $\partial u/\partial y$) were studied using their probability density functions (PDFs). They

TABLE I
Isotropy of the Fields at t = 0 s

$\measuredangle(z, \zeta)$	$\langle u_i^2 \rangle / \sum \langle u_i^2 \rangle$	$\langle \omega_i^2 \rangle / \sum \langle \omega_i^2 \rangle$	$\langle \omega^2 \rangle / \langle \mathrm{tr}(s^2) \rangle$
64^3 grid nodes			
0°	0.334, 0.292, 0.373	0.353, 0.323, 0.323	2.000
	0.328, 0.308, 0.365	0.334, 0.341, 0.325	2.000
	0.308, 0.283, 0.409	0.366, 0.352, 0.281	2.000
15°	0.334, 0.292, 0.373	0.353, 0.323, 0.324	2.000
	0.327, 0.308, 0.365	0.334, 0.341, 0.325	2.000
	0.308, 0.283, 0.410	0.367, 0.352, 0.282	2.000
30°	0.334, 0.292, 0.373	0.353, 0.323, 0.324	2.000
	0.327, 0.308, 0.365	0.334, 0.340, 0.326	1.999
	0.308, 0.283, 0.410	0.366, 0.352, 0.282	2.000
45°	0.334, 0.292, 0.373	0.352, 0.322, 0.326	1.998
	0.327, 0.307, 0.366	0.333, 0.340, 0.327	1.997
	0.307, 0.282, 0.411	0.366, 0.351, 0.283	1.998
128^3 grid nodes			
0°	0.323, 0.321, 0.356	0.358, 0.290, 0.353	2.000
15°	0.323, 0.321, 0.356	0.358, 0.290, 0.353	2.000
30°	0.323, 0.321, 0.356	0.358, 0.290, 0.353	2.000
45°	0.323, 0.321, 0.356	0.358, 0.289, 0.353	2.000

Note. Each line corresponds to one simulation.

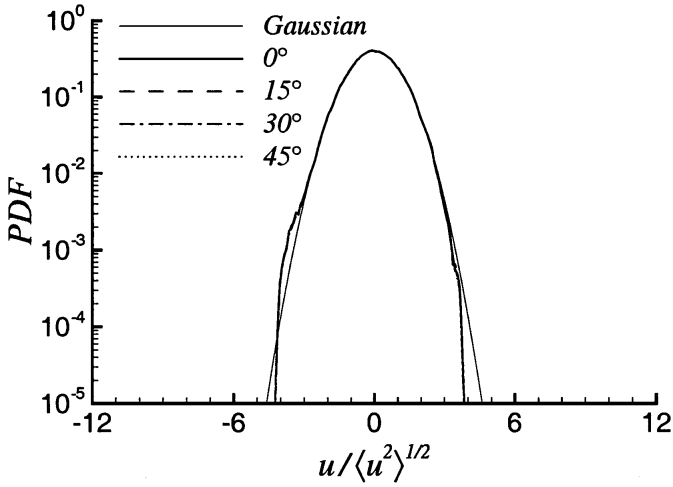

FIG. 9. PDF of the normalized velocity field at $t = 0$ s (64^3 grid nodes), shown together with a Gaussian distribution.

should be near Gaussian, as a consequence of the procedure that we used to generate the initial fields. The statistical distributions were determined based on the assumption that the fields were isotropic. This enabled us to increase the sample size, using, for instance, the three velocity components u, v, and w, for calculating the PDF of u.

The statistical distribution of the initial velocity field (Fig. 9) and velocity derivatives (Fig. 10) were near Gaussian and did not show any influence from the grid distortion. The results were identical despite the various distortions tested and collapsed to a single line. Because the same holds in the case of the grid with 128^3 nodes, the figures are not included here.

Figure 11 shows that there was a good agreement between the calculated values and the theoretical dissipation spectra, $D(k) = 2\nu Ak^6 \exp(-Bk^2)$, as derived from the energy spectra (15).

We also looked at the eigenvalues of the rate of strain tensor s_{ij} (λ_1, λ_2, and λ_3). Continuity implies that $\lambda_1 + \lambda_2 + \lambda_3 = 0$. If λ_1 is the lowest and always negative and λ_3 the greatest and

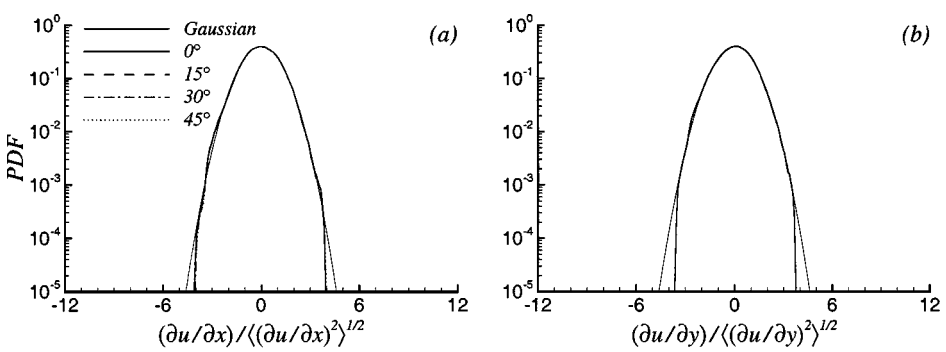

FIG. 10. PDFs of the normalized (a) longitudinal and (b) lateral velocity derivatives field at $t = 0$ s (64^3 grid nodes), shown together with a Gaussian distribution.

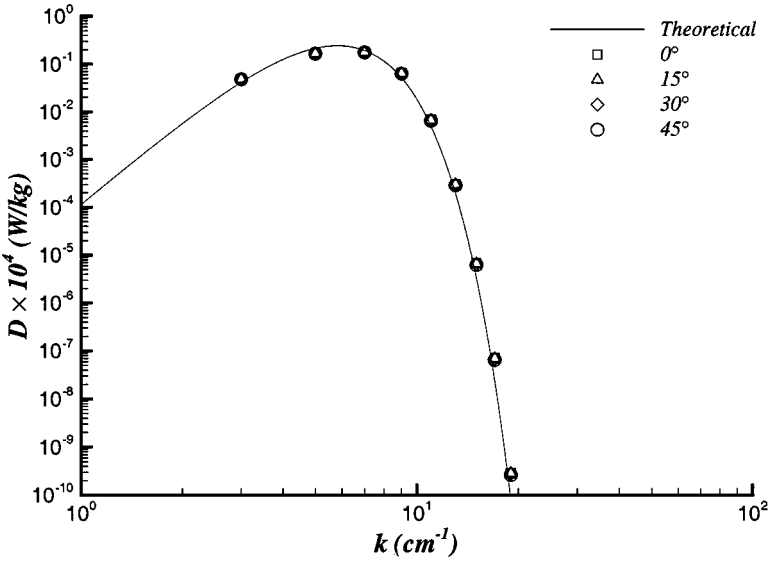

FIG. 11. Dissipation spectra at $t = 0$ s (64^3 grid nodes).

always positive, λ_2 is positive or negative, depending on whether $|\lambda_1| > |\lambda_3|$ or $|\lambda_1| < |\lambda_3|$. Given the randomness of the initial fields, it was expected that λ_2 would be positive in between approximately 50% of the domain. In our calculations λ_2 was positive between 48 and 52% of the domain and no difference was found between the orthogonal and the nonorthogonal domains.

The alignment between the vorticity and the directions of the principal rates of strain of the initial fields was also verified. If $\mathbf{e_1}$, $\mathbf{e_2}$, and $\mathbf{e_3}$ are the eigenvectors associated with the eigenvalues λ_1, λ_2, and λ_3, the angle θ_i between the vorticity vector and the direction of the principal rate of strain represented by the eigenvector $\mathbf{e_i}$ is defined by

$$\theta_i = \arccos \frac{|\boldsymbol{\omega} \cdot \boldsymbol{e_i}|}{\|\boldsymbol{\omega}\| \|\boldsymbol{e_i}\|}. \tag{28}$$

Because the initial fields were the result of a random process, it was expected that the PDF of θ_1, θ_2, and θ_3 would be identical to the PDF of the angle between a random vector and a random direction. All the PDFs showed that angles greater than 50° were more frequent than in the random case (Fig. 12). However, they did not change with the domain distortion.

3.4. Time Development of Statistical Parameters

The ratio Q_2 between the Fourier modes of the discretized and of the exact derivative was introduced in Section 3.2.1. However, a precise error estimation should consider also the shape of the energy spectrum. The parameter $\epsilon(t)$, defined by

$$\epsilon^2(t) = \frac{\int (1 - Q_2)^2 k_z^2 E(k, t)\, \mathrm{d}k}{\int k_z^2 E(k, t)\, \mathrm{d}k},$$

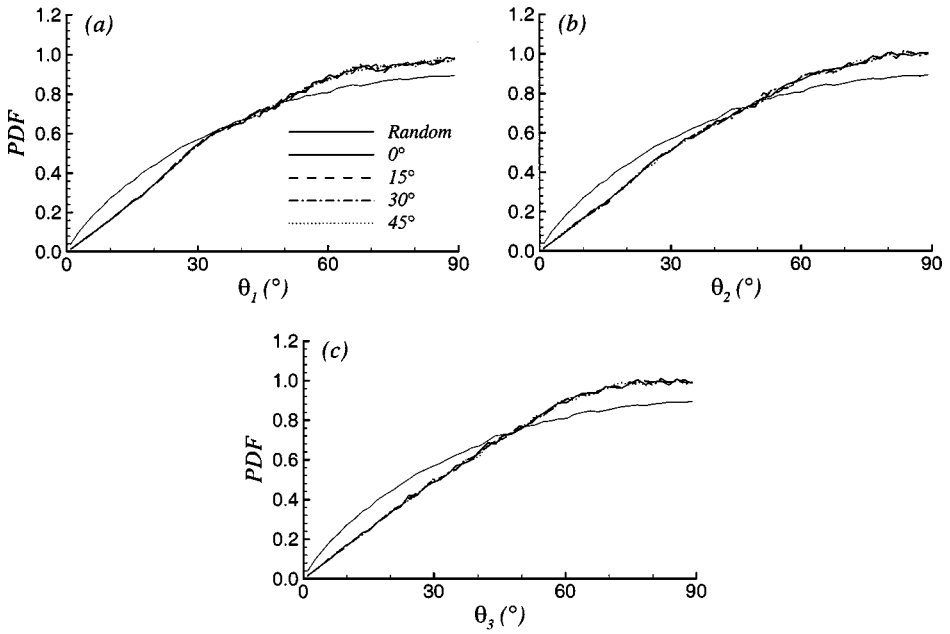

FIG. 12. PDFs of the angles between the vorticity and the directions of principal rates of strain at $t = 0$ s (64^3 grid nodes), shown together with the PDFs of the angles between a random vector and a random direction.

measures the error of discretization of derivatives with respect to the Cartesian direction z at each time step (cf. [4]).

The error ϵ increased with time until $t \approx 0.5$ (Fig. 13), accompanying the energy transfer from low to high wave numbers. The error does not increase linearly with the distortion: the domains with $\alpha = 15$ and 30° display errors 2 and 5% higher than in the orthogonal case, whereas for $\alpha = 45^\circ$ it can exceed the undistorted case by up to 10%. ϵ appears to be correlated with the average accuracy for each wave number, which degrades with increasing grid distortion (Figs. 5 and 6), rather than with the accuracy of some individual Fourier modes, which was worst for $\alpha = 15$ or 30° (Fig. 4).

Considering the temporal evolution of the turbulence kinetic energy (Fig. 14), the domain with 45° of distortion had always the lowest energy. At the end of the simulations ($t = 0.8$ s)

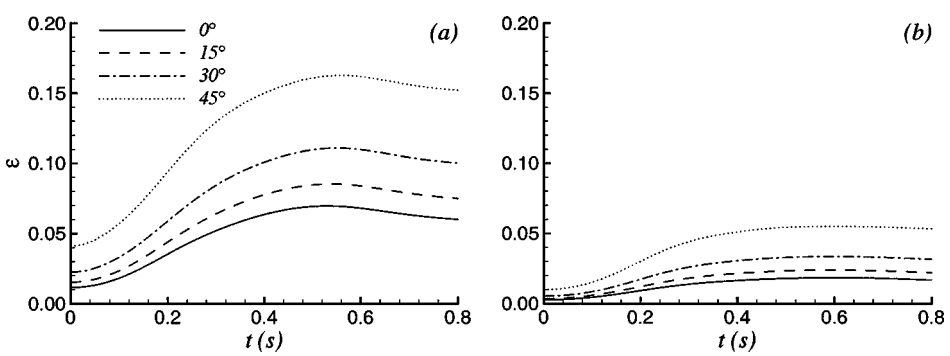

FIG. 13. Temporal evolution of the error of discretization of derivatives with respect to the Cartesian direction z at each time step. (a) 64^3 grid nodes and (b) 128^3 grid nodes.

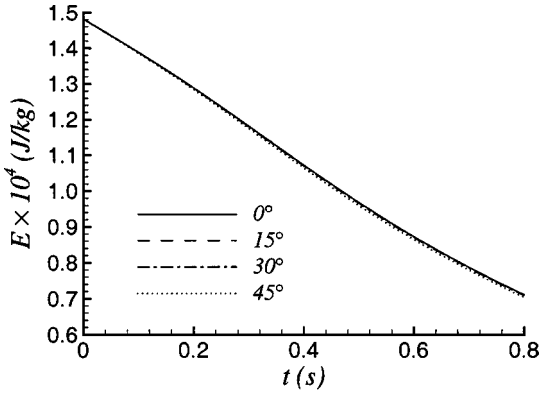

FIG. 14. Temporal evolution of the turbulence kinetic energy (64^3 grid nodes).

its total energy was 1% less than in the orthogonal domain, which had always the highest energy. The decay in the domain with 15° of distortion was the closest to the orthogonal domain, with a difference of less than 0.05% at the end of the simulation. This behavior was somehow expected because of the increased lack of conservation introduced by the calculation of the mass fluxes at the cell surfaces (Eq. (13)) and because of the higher discretization errors in more distorted domains.

The skewness of the longitudinal velocity derivative, defined by

$$S_{\partial u/\partial x} = -\frac{\langle(\partial u/\partial x)^3\rangle}{\langle(\partial u/\partial x)^2\rangle^{1.5}},$$

is a nondimensional measure of enstrophy production and energy transfer due to the nonlinear interaction and, therefore, a parameter of crucial importance in the simulation of turbulence. Its evolution in the orthogonal domain (Fig. 15) was identical to that reported in Ref. [18]. In all calculations, the skewness required about half of the eddy turnover time before reaching a plateau of about 0.5. The evolution in the distorted domains could differ up to 3% from that in the orthogonal domain, which we considered acceptable, because it was smaller than the differences observed between the three simulations in the orthogonal domain with the 64^3 grid.

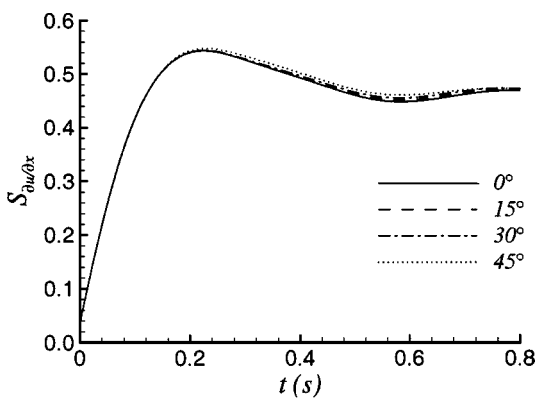

FIG. 15. Temporal evolution of the skewness of the longitudinal velocity derivatives (64^3 grid nodes).

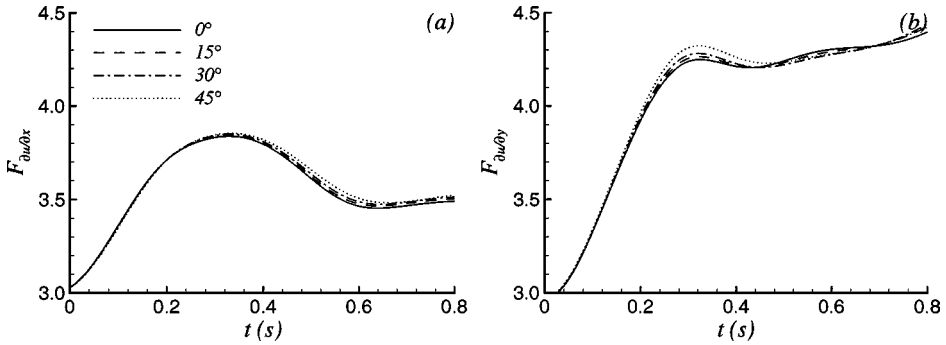

FIG. 16. Temporal evolution of the flatness (64^3 grid nodes) of the (a) longitudinal and (b) lateral velocity derivatives.

The flatness of the longitudinal and lateral velocity derivatives,

$$F_{\partial u/\partial x} = \frac{\langle(\partial u/\partial x)^4\rangle}{\langle(\partial u/\partial x)^2\rangle^2},$$

$$F_{\partial u/\partial y} = \frac{\langle(\partial u/\partial y)^4\rangle}{\langle(\partial u/\partial y)^2\rangle^2},$$

can provide information on how the vorticity is aligned with the rate of strain [24].

The temporal evolution of the flatness was identical in all domains (Fig. 16). The difference between the domains was less than 2%, a value also smaller than that observed between the simulations started with different initial velocity fields in the orthogonal domain.

We noticed, in accordance with Ref. [26], that the flatness of the lateral velocity derivative (Fig. 16b) was higher than that of the longitudinal derivative (Fig. 16a). However, in the case reported by Ref. [26], with $Re_\lambda \approx 150$, the values are higher ($F_{\partial u/\partial x} = 5.9$ and $F_{\partial u/\partial y} = 8$) than these reported here ($F_{\partial u/\partial x} = 3.6$ and $F_{\partial u/\partial y} = 4.5$). The value of $F_{\partial u/\partial x}$ agrees with the one reported by Ref. [11] for $Re_\lambda = 40$, as in the current study.

At the end of the simulations, $t = 0.8$ s, the turbulent Reynolds dropped to half its initial value, and the differences between results on different domains were less than 3% (Fig. 17).

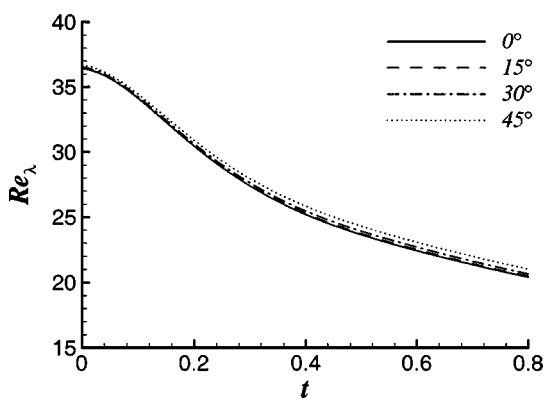

FIG. 17. Temporal evolution of the turbulent Reynolds number (64^3 grid nodes).

TABLE II
Isotropy of the Fields at $t = 0.8$ s

$\measuredangle(z, \zeta)$	$\langle u_i^2\rangle / \Sigma\langle u_i^2\rangle$	$\langle \omega_i^2\rangle / \Sigma\langle \omega_i^2\rangle$	$\langle \omega^2\rangle / \langle \mathrm{tr}(s^2)\rangle$
64^3 grid nodes			
0°	0.351, 0.301, 0.348	0.345, 0.329, 0.326	2.000
	0.300, 0.324, 0.376	0.367, 0.321, 0.313	2.000
	0.317, 0.295, 0.387	0.353, 0.316, 0.331	2.000
15°	0.351, 0.301, 0.347	0.345, 0.328, 0.327	2.000
	0.300, 0.324, 0.376	0.369, 0.319, 0.313	2.000
	0.317, 0.296, 0.387	0.353, 0.316, 0.332	2.000
30°	0.352, 0.302, 0.346	0.346, 0.326, 0.328	2.000
	0.300, 0.326, 0.375	0.371, 0.314, 0.314	2.000
	0.317, 0.296, 0.387	0.354, 0.317, 0.333	2.000
45°	0.354, 0.303, 0.344	0.349, 0.322, 0.329	2.000
	0.300, 0.329, 0.371	0.379, 0.304, 0.317	2.000
	0.317, 0.297, 0.386	0.358, 0.307, 0.335	2.000
128^3 grid nodes			
0°	0.301, 0.320, 0.380	0.320, 0.321, 0.359	2.000
15°	0.301, 0.320, 0.380	0.320, 0.321, 0.359	2.000
30°	0.301, 0.320, 0.379	0.321, 0.320, 0.360	2.000
45°	0.301, 0.320, 0.379	0.322, 0.318, 0.360	2.000

Note. Each line corresponds to one simulation, as in Table I.

3.5. Fields after the Decay

In the previous section we considered the temporal evolution of statistical parameters; here we present some results obtained at the end of the simulations ($t = 0.8$ s).

Isotropy was first checked in the large and small scales (velocity and vorticity) and by the isotropic relation (27), shown in Table II. The fields at $t = 0.8$ s in the nonorthogonal domains seemed as equally isotropic as the fields in the orthogonal domain. The isotropic relation (27) was always satisfied to the third decimal figure, which did not always occur at $t = 0$ s (see Table I).

The PDFs of the velocity field were all identical and near Gaussian (Fig. 18), as is known from previous simulations [23]. The pressure PDFs were also very similar and, as in

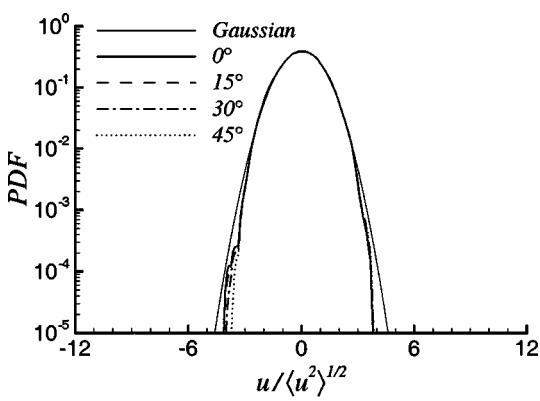

FIG. 18. PDF of the normalized velocity field at $t = 0.8$ s (64^3 grid nodes), shown together with a Gaussian distribution.

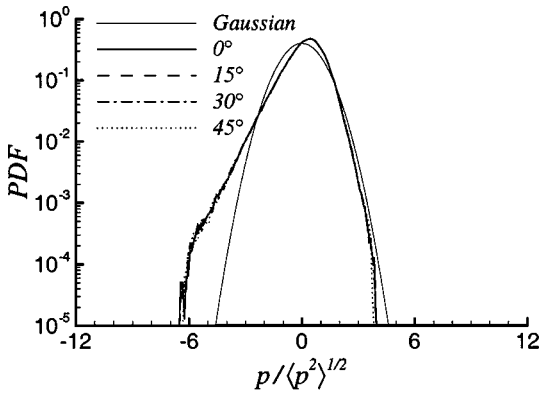

FIG. 19. PDF of the normalized pressure field at $t = 0.8$ s (64^3 grid nodes), shown together with a Gaussian distribution.

Ref. [15], exponential in the lows and Gaussian in the highs (Fig. 19). This was reproduced in all domains.

The PDFs of the longitudinal and lateral velocity derivatives (Fig. 20) in the different domains were also in agreement with each other. Some scatter was visible in the tails, attributable to the limited sample size.

There was also good agreement between the dissipation spectra, regardless of the domain distortion (Fig. 21). The spectra calculated in the grid with 64^3 nodes was similar, but with a lower cutoff.

Kerr [11] found and Vincent and Meneguzzi [26] confirmed that, in general, the largest rate of strain was compressive and perpendicular to the vorticity, the smaller stretching was aligned with the vorticity, and the larger stretching was perpendicular to the vorticity. To see whether the different domain distortions altered these correlations, we studied the PDFs of the angles θ_i, defined in (28). In absolute value, λ_1 was the largest principal rate of strain in approximately 77% of the domain points, for all domain distortions and with either 64^3 or 128^3 grids. This value was higher than the 67% reported in Ref. [26], despite their higher Re_λ ($\approx$150). The PDFs of θ_i showed that the domain distortion did not affect the alignment between the vorticity and the rate of strain (Fig. 22). In case of the θ_1 PDF, angles greater than 65° were more frequent than in the random distribution (Fig. 22a), while the θ_2 PDF indicated that angles inferior to 45° were more probable (Fig. 22b). The θ_3 PDF, opposed

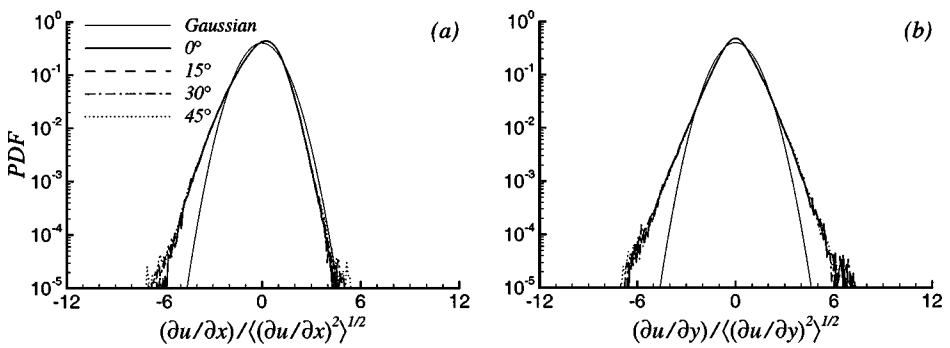

FIG. 20. PDFs of the normalized (a) longitudinal and (b) lateral velocity derivatives field at $t = 0.8$ s (64^3 grid nodes), shown together with a Gaussian distribution.

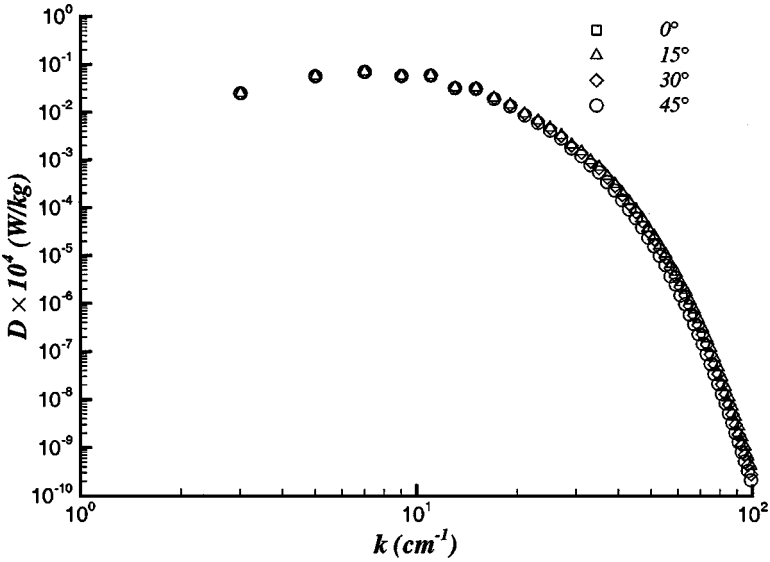

FIG. 21. Dissipation spectra at $t = 0.8$ s (128^3 grid nodes).

to the θ_1 and θ_2 PDF, changed little since $t = 0$ s (Fig. 12c) and showed that angles greater than 60° were more frequent than in the random case (Fig. 22c).

Finally, a comparison of one component of the vorticity field at the end of the simulation was included (Fig. 23). Even if the domain distortion (Fig. 13) could increase almost three times the error of spatial discretization of derivatives in the domain with $\alpha = 45°$, Fig. 23 and the foregoing analysis showed that the same flow was simulated on the various domains.

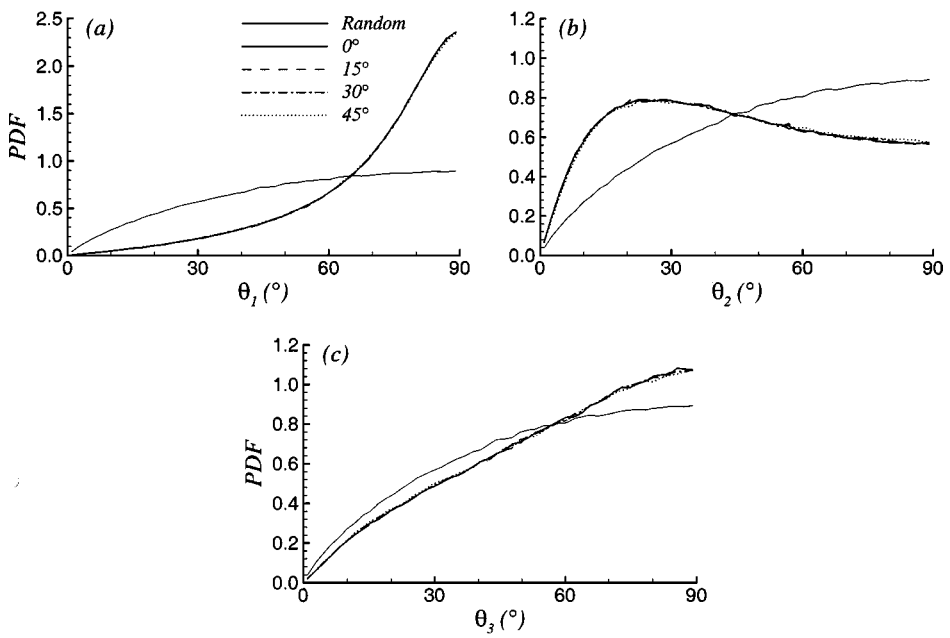

FIG. 22. PDFs of the angles between the vorticity and the directions of the principal rates of strain at $t = 0.8$ s (64^3 grid nodes), shown together with the PDFs of the angle between a random vector and a random direction.

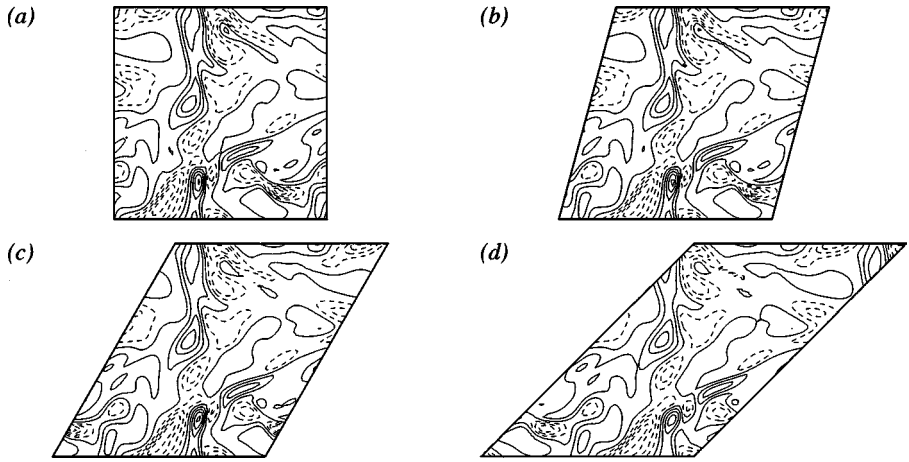

FIG. 23. ω_y vorticity field in a xz plane at $t = 0.8$ s (64^3 grid nodes). (a) $\alpha = 0°$; (b) $\alpha = 15°$; (c) $\alpha = 30°$; (d) $\alpha = 45°$.

4. CONCLUSIONS

The purpose of this work was to study the influence of a nonorthogonal grid in the numerical simulation, based on the finite-volume methodology, of decaying isotropic turbulence. Four different domains—distinct in the angle between the computational direction ζ and the physical direction z—were considered: 0 (orthogonal domain, used as reference), 15, 30, and 45°.

The simulations started from random velocity fields, identical for all grid distortions and generated with imposed correlations and spectra. It was observed that, as opposed to what occurs with a Cartesian grid, with a nonorthogonal grid the Fourier modes of the discretized derivatives could be amplified or have inverted phase, relatively to the modes of the exact derivative. However, the average accuracy for each wave number degrades slowly with increasing grid distortion and seems to be a better indicator of the spatial discretization error than the accuracy of individual Fourier modes.

During the turbulence decay the fields were identical, regardless of the grid distortion. The differences in the skewness of the longitudinal velocity derivative $\partial u/\partial x$ (related to the energy transfer) and in the flatness of the longitudinal and lateral velocity derivative $\partial u/\partial y$ (related to the alignment of vorticity and rate of strain) were less than 3%.

At the end of the simulation ($t = 0.8$ s), the difference in the turbulence kinetic energy was 1%. The distortion of the domain affected neither the isotropy of the flow nor the alignment between the vorticity and the rate of strain. In general, the vorticity was aligned with the second principal rate of strain and was perpendicular to the others.

As a general conclusion, the grid nonorthogonality does not seem to affect the numerical simulation of decaying isotropic turbulence and the methodology presented here may be extended to more complex problems and geometries.

APPENDIX

The set of equations defining the third-order Runge–Kutta scheme with four substeps, Runge–Kutta (4,3), is

$$\phi^*_{n+\frac{19}{36}} = \phi^n + \frac{19}{36}\Delta t \cdot f(t_n, \phi^n); \qquad f^* = f\left(t_{n+\frac{19}{36}}, \phi^*_{n+\frac{19}{36}}\right) - \frac{205}{243} f(t_n, \phi^n);$$

$$\phi^*_{n+\frac{3}{4}} = \phi^*_{n+\frac{19}{36}} + \frac{27}{19}\Delta t \cdot f^*; \qquad f^{**} = f\left(t_{n+\frac{3}{4}}, \phi^*_{n+\frac{3}{4}}\right) - \frac{243}{38} f^*;$$

$$\phi^{**}_{n+\frac{3}{4}} = \phi^*_{n+\frac{3}{4}} + \frac{2}{9}\Delta t \cdot f^{**}; \qquad f^{***} = f\left(t_{n+\frac{3}{4}}, \phi^{**}_{n+\frac{3}{4}}\right) - \frac{2}{9} f^{**};$$

$$\phi^{n+1} = \phi^{**}_{n+\frac{3}{4}} + \frac{1}{4}\Delta t \cdot f^{***}.$$

ACKNOWLEDGMENTS

This work was performed under research contract PRAXIS XXI, number EMG/1967/95. A. Silva Lopes acknowledges support through grant PRAXIS XXI/BD/3990/94. The authors are grateful to their colleague S. Gama for his comments and discussion on a previous version of this work. The comments and suggestions of two anonymous reviewers contributed also to the improvement of the paper. The current work benefited from the sabbatical leave of the second author at the Institute of Atmospheric Physics of the DLR, in Wessling, Germany, a few years ago and from discussions being held with Dr. Thomaz Gerz and Professor Ulrich Schumann, to whom we express our gratitude.

REFERENCES

1. AGARD, *A Selection of Test Cases for the Validation of Large-Eddy Simulations of Turbulent Flows*, Technical Report AGARD-AR-345 (NATO, 1998).
2. R. Anderson and C. Meneveau, Effects of the similarity model in finite-difference LES of isotropic turbulence using a Lagrangian dynamic mixed model, *Flow Turbulence Combust*. **62**, 201 (1999).
3. M. H. Carpenter and C. A. Kennedy, *Fourth-Order 2N-Storage Runge-Kutta Schemes*, Technical Report NASA-TM-109112 (NASA Langley Research Center, 1994).
4. J. H. Ferziger and M. Perić, *Computational Methods for Fluid Dynamics* (Springer-Verlag, Berlin/New York, 1999), 2nd ed.
5. S. Ghosal, An analysis of numerical errors in large-eddy simulations of turbulence, *J. Comput. Phys.* **125**, 187 (1996).
6. J. R. Herring, S. A. Orszag, R. H. Kraichnan, and D. G. Fox, Decay of two-dimensional homogeneous turbulence, *J. Fluid Mech*. **66**, 417 (1974).
7. J. Jiménez and A. A. Wray, The structure of intense vorticity in isotropic turbulence, *J. Fluid Mech*. **373**, 255 (1998).
8. J. Jiménez, A. A. Wray, P. G. Saffman, and R. Rogallo, On the characteristics of vortex filaments in isotropic turbulence, *J. Fluid Mech*. **255**, 65 (1993).
9. S. A. Jordan, A large-eddy simulation methodology in generalized curvilinear coordinates, *J. Comput. Phys.* **148**, 322 (1999).
10. H.-J. Kaltenbach, Cell aspect ratio dependence of anisotropy measures for resolved and subgrid scale stresses, *J. Comput. Phys*. **136**, 399 (1997).
11. R. M. Kerr, Higher-order derivative correlations and the alignment of small-scale structures in isotropic numerical turbulence, *J. Fluid Mech*. **153**, 31 (1985).
12. J. Kim and P. Moin, Application of a fractional-step method to incompressible Navier-Stokes equations, *J. Comput. Phys*. **59**, 308 (1985).
13. A. G. Kravchenko and P. Moin, On the effect of numerical errors in large eddy simulations of turbulent flows, *J. Comput. Phys*. **131**, 310 (1997).
14. S. K. Lele, Compact finite difference schemes with spectral-like resolution, *J. Comput. Phys*. **103**, 16 (1992).
15. O. Métais and M. Lesieur, Spectral large-eddy simulation of isotropic and stably stratified turbulence, *J. Fluid Mech*. **239**, 157 (1992).
16. P. Moin and K. Mahesh, Direct numerical simulation: A tool in turbulence research, *Annu. Rev. Fluid Mech.* **30**, 539 (1998).

17. Y. Morinishi, T. S. Lund, O. V. Vasilyev, and P. Moin, Fully conservative higher order finite difference schemes for incompressible flow, *J. Comput. Phys*. **143**, 90 (1998).
18. S. A. Orszag and G. S. Patterson, Numerical simulation of three-dimensional homogeneous isotropic turbulence, *Phys. Rev. Lett*. **28**, 76 (1972).
19. M. M. Rai and P. Moin, Direct simulation of turbulent flow using finite-difference schemes, *J. Comput. Phys*. **96**, 15 (1991).
20. W. C. Reynolds, in *Whither Turbulence? Turbulence at the Crossroads*, edited by J. Lumley (Springer-Verlag, Berlin/New York, 1989), pp. 313–343.
21. C. M. Rhie and W. L. Chow, Numerical study of the turbulent flow past an airfoil with trailing edge separation, *AIAA J*. **21**, 1525 (1983).
22. U. Schumann, in *Proceedings of the Nineth International Conference on Numerical Methods in Fluid Dynamics*, edited by J. P. Soubbaramayer and J. P. Boujot (Springer-Verlag, Berlin/Heidelberg, 1985), pp. 492–496.
23. U. Schumann, and G. S. Patterson, Numerical study of pressure and velocity fluctuations in nearly isotropic turbulence, *J. Fluid Mech*. **88**, 685 (1978).
24. E. D. Siggia, Numerical study of small-scale intermittency in three-dimensional turbulence, *J. Fluid Mech*. **107**, 375 (1981).
25. A. Silva Lopes, *Flow Simulation in Complex Geometries by Large Eddy Simulation* (in Portuguese), Ph.D. thesis (Univ. Porto, Portugal, 2000).
26. A. Vincent and M. Meneguzzi, The spatial structure and statistical properties of homogeneous turbulence, *J. Fluid Mech*. **225**, 1 (1991).
27. Y. Zhang, R. L. Street, and R. Koseff, A non-staggered grid, fractional step method for time-dependent incompressible Navier–Stokes equations in curvilinear coordinates, *J. Comput. Phys*. **114**, 18 (1994).